Materials Advances

ROYAL SOCIETY OF CHEMISTRY

PAPER

View Article Online
View Journal | View Issue

Cite this: *Mater. Adv.*, 2023, 4, 6389

Radiosensitizing molybdenum iodide nanoclusters conjugated with a biocompatible *N*-(2-hydroxypropyl)methacrylamide copolymer: a step towards radiodynamic therapy†

Kaplan Kirakci, *[a] Robert Pola, *[b] Marina Rodrigues Tavares,[b] Michal Pechar,[b] Tomáš Přibyl,[c] Ivana Křížová,[c] Jaroslav Zelenka,[c] Tomáš Ruml,[c] Tomáš Etrych[b] and Kamil Lang[a]

Received 22nd August 2023,
Accepted 2nd November 2023

DOI: 10.1039/d3ma00577a

rsc.li/materials-advances

Radiodynamic therapy treats deep-seated tumors by exploiting radiosensitizers (RSs) that are delivered to tumors and produce reactive oxygen species upon X-ray irradiation. Octahedral molybdenum clusters (Mo_6) have shown promise as RSs, but their direct administration is hampered by their limited stability and low solubility in the biological medium. Association of the Mo_6 clusters with organic polymers can overcome this issue and improve their bioavailability. Herein, we have conjugated a dibenzocyclooctyne-functionalized *N*-(2-hydroxypropyl)methacrylamide copolymer with a Mo_6 cluster bearing azido ligands *via* a copper-free click reaction. The resulting nanosized Mo_6 cluster/polymer conjugate exhibited long-term stability of its colloidal and luminescence properties in phosphate-buffered saline, and displayed photosensitized formation of singlet oxygen, affirming its potential for photodynamic processes. The conjugate was not toxic towards HeLa cells, demonstrated phototoxic effects upon blue-light irradiation, with an better therapeutic window than the bare Mo_6 cluster, and showed promise as an RS, enhancing cell growth suppression upon X-ray irradiation. Overall, this nanosystem constitutes a propitious theranostic tool for photo/radiodynamic applications.

Introduction

The convergence of photodynamic therapy (PDT) and radiotherapy has given rise to a modality called radiodynamic therapy (RDT). RDT is based on the tumoral delivery of molecules or nanomaterials, so called radiosensitizers (RSs), which produce reactive oxygen species (ROS) upon X-ray irradiation. PDT is limited to tumors located on the surface or a few millimeters under the skin or inside cavities due to the limited penetration of visible light through living tissues. RDT overcomes this obstacle allowing the treatment of deep-seated tumors and, at the same time, decreasing the radiation doses needed to reach anti-proliferative effects in the frame of a radiotherapy treatment. The initial proof-of-principle relied on a radiosensitizing system constructed from scintillating nanoparticles excited *via* resonance energy transfer of porphyrinic photosensitizers to produce ROS, immobilized within pores of a surrounding mesoporous silica shell.[1] Since then, several research groups have reported alternative approaches that simplify the use of RDT for cancer treatment.[2–6] For instance, semiconducting[7] or gold[8] nanoparticles directly produce ROS, such as hydroxyl radicals or superoxide radical-anions, upon X-ray irradiation. In addition, the X-ray induced production of singlet oxygen, $O_2(^1\Delta_g)$, can be achieved through the use of RSs made of high-*Z* elements, such as octahedral molybdenum clusters (Mo_6).[9]

Mo_6 clusters are octahedra of molybdenum atoms stabilized by eight strongly bonded halogen inner ligands and six labile inorganic/organic apical ligands (L). They display red phosphorescence, and produce $O_2(^1\Delta_g)$ in high yields.[10] Recently, we discovered that Mo_6 clusters of the $[Mo_6I_8L_6]^n$ type function as X-ray scintillators, thanks to their constituting high-Z elements, and also suggested that these clusters can radiosensitize the production of $O_2(^1\Delta_g)$.[9] This last feature was later confirmed as we demonstrated the ability of Mo_6 clusters to enhance radiation effects *in vitro*.[11,12] In addition, the possibility to coordinate a wide range of apical ligands allows for targeting specific cellular organelles sensitive to $O_2(^1\Delta_g)$.[13–15] *In vivo* experiments with Mo_6 clusters evidenced their low toxicity with regards to typical concentrations used in RDT.[11,12] Thus, biomaterials based on Mo_6 clusters represent good candidates for applications in RDT.

[a] *Institute of Inorganic Chemistry of the Czech Academy of Sciences, 250 68 Husinec-Řež, Czech Republic. E-mail: kaplan@iic.cas.cz*
[b] *Institute of Macromolecular Chemistry of the Czech Academy of Sciences, Heyrovského náměstí 2, 162 00 Prague 6, Czech Republic. E-mail: pola@imc.cas.cz*
[c] *Department of Biochemistry and Microbiology, University of Chemistry and Technology Prague, Technická 5, 166 28 Praha 6, Czech Republic*

† Electronic supplementary information (ESI) available: DLS, phosphorescence signal of $O_2(^1\Delta_g)$, additional phosphorescence spectra, flow cytometry, toxicity and phototoxicity without FBS. See DOI: https://doi.org/10.1039/d3ma00577a

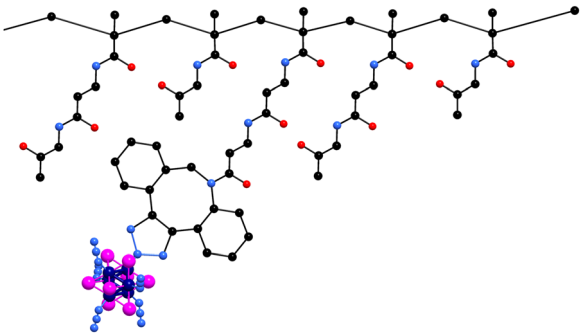

Fig. 1 Schematic representation of the cluster/polymer conjugate (color coding: molybdenum in dark blue, iodine in magenta, carbon in black, oxygen in red, and nitrogen in light blue); hydrogen atoms were omitted for clarity.

The direct administration of Mo_6 clusters is not pertinent owing to their partial coordination instability in aqueous media. This results in the displacement of apical ligands by water molecules, causing aggregation, and worsening sensitizing and cellular uptake properties. Even though hydrolysis can be mitigated by using bulky hydrophobic apical ligands, these clusters then display poor water solubility, thus limiting their deposition at tumor sites.[12,14,16] Nanosystems prepared using natural or synthetic polymers can be used to overcome this drawback as these colloidal carriers can facilitate the delivery of a wide variety of therapeutic molecules for the medical treatment of numerous diseases.[17,18] Such polymer-based nanosystems have also gained attention for the treatment of tumors as they exhibit appropriate pharmacokinetic properties, low toxicity, and therapeutic efficacy due to the enhanced permeability and retention effect.[19] In this respect, *N*-(2-hydroxypropyl)methacrylamide (HPMA) copolymers have already been engineered and applied to increase the stability of Mo_6 clusters in water, which might also improve their bioavailability.[20]

Herein, we report on the photo/radiosensitizing activity of a HPMA-based conjugate with the Mo_6 cluster, $Na_2[Mo_6I_8(N_3)_6]$, covalently bound *via* a copper-free azide–alkyne click chemistry (Fig. 1). The content of molybdenum of the conjugates was measured using inductively coupled plasma mass spectrometry (ICP-MS). The enhancement of the aqueous colloidal and photophysical stability of the cluster upon conjugation was evaluated by dynamic light scattering and luminescence spectroscopy in PBS. The biological activity of the conjugate was tested on HeLa cells by means of uptake, toxicity, phototoxicity, photoinduced ROS production, cell death mode, and radiotoxicity experiments.

Materials and methods

Reagents and general procedures

Compound $Na_2[\{Mo_6I_8\}(N_3)_6]$ (**1**) was prepared according to a previously published procedure.[21] Molybdenum, iodine, and sodium azide were obtained from Sigma Aldrich and used as received. Solvents for the synthesis of clusters were purchased from Penta (Czech Republic) and dried over molecular sieves (3 Å). 1,4-Dioxane, 2,2′-azobisisobutyronitrile (AIBN), 2-cyanopropan-2-yl dithiobenzoate (CTA-AIBN), 2-thiazoline-2-thiol, 2,4,6-trinitrobenzene-1-sulfonic acid (TNBSA), 3-azido-1-propylamine, 4,4′-azobis(4-cyanopentanoic acid) (ACVA), 4-cyano-4-(thiobenzoylthio)-pentanoic acid (CTA-ACVA), dimethyl sulfoxide (DMSO), methacryloyl chloride, *N*,*N*-di*iso*-propylethylamine (DIPEA), *N*,*N*-dimethylacetamide (DMA), phosphate buffered saline (phosphate buffer 0.01 M and NaCl 0.154 M, and pH 7.4) (PBS), and *tert*-butanol were purchased from Sigma-Aldrich (Prague, Czech Republic). 2,2′-Azobis(4-methoxy-2,4-dimethylvaleronitrile) (V-70) was from Fujifilm Wako Chemicals Europe (Neuss, Germany). 3-Amino-1-(11,12-didehydrodibenzo[*b*,*f*]azocin-5(6*H*)-yl)propan-1-one (DBCO-NH_2) was from Click Chemistry Tools (Scottsdale, AZ, USA). All solvents and chemicals were of analytical grade.

Synthesis of poly(HPMA-*co*-MA-β-Ala-DBCO)

Precursor poly(HPMA-*co*-MA-β-Ala-TT) containing reactive thiazolidine-2-thione (TT) groups was prepared by the controlled radical reversible addition–fragmentation chain transfer (RAFT) polymerization, using HPMA and *N*-methacryloyl-β-alanine thiazolidine-2-thione (MA-β-Ala-TT) as previously described.[20] The molar ratio of HPMA/MA-β-Ala-TT was 80/20 and the reaction mixture contained 0.9 M solution of monomers. The molar ratio monomer/chain transfer agent/AIBN was 650/2/1.

Polymer precursors bearing 8 mol% of DBCO groups poly(HPMA-*co*-MA-β-Ala-DBCO) were synthesized *via* aminolysis of TT groups from poly(HPMA-*co*-MA-β-Ala-TT) with DBCO-NH_2 in DMA using DIPEA. The unreacted TT groups were removed with 1-aminopropan-2-ol. The reaction conditions were adopted from our previous work.[20]

Synthesis of a poly(HPMA-*co*-MA-β-Ala-DBCO)/$Na_2[Mo_6I_8(N_3)_6]$ conjugate (2)

The conjugate was prepared *via* a copper-free click reaction, adapted from our previous work.[20] The precursor poly(HPMA-*co*-MA-β-Ala-DBCO) with 8 mol% of DBCO (20 mg, 10.3 μmol of DBCO group) was dissolved in DMSO (1 mL) then added into a solution of $Na_2[Mo_6I_8(N_3)_6]$ (**1**) (200 mg, 106 μmol) in DMSO (1 mL) under stirring. After 4 days under stirring at room temperature, 45 mL of diethyl ether were added to the reaction mixture and the resulting orange precipitate was washed 3 times with 5 mL of acetone to remove unbound clusters. The remaining orange solid was washed with 20 mL of diethyl ether and dried under reduced pressure.

Toxicity and phototoxicity

Human cervical adenocarcinoma cells (HeLa) were cultured in EMEM medium (Sigma-Aldrich) supplemented with 0.5 mM glutamine and 5% (*V*/*V*) fetal bovine serum (FBS) (full medium) at 37 °C in a CO_2 (5%) incubator. Experiments were performed 24 h after seeding. The medium was exchanged for the phenol red-free full medium or phenol red-free full medium without FBS, and **1** or **2** dissolved in water was added. After 24 h, cells were irradiated or kept in the dark. Irradiation was performed with a 12 × 10 LED source (Cameo) at 460 nm for 15 min (18 mW cm^{-2}). The resazurin assay was utilized for the cell viability analysis. In control experiments, cells were treated with water, otherwise the experimental conditions were the same.

Cellular death

HeLa cells were seeded in a 12-well plate in the full medium. The next day, the cells were treated with **1** or **2** at a concentration of 200 μg mL^{-1} and incubated for the next 24 h. Then, the cells were irradiated at 460 nm for 15 min (18 mW cm^{-2}). After 4 h, the wells were washed with PBS, trypsinized, again washed with PBS and processed according to the manufacturer's protocol for the Dead Cell Apoptosis Kit (Invitrogen), and analyzed by flow cytometry (BD FACSaria III).

ROS level determination in cells

HeLa cells were seeded in a 96-well plate in the full medium. The next day, the medium was exchanged for fresh full medium and treated with **1** or **2** at the indicated concentrations. 24 h after incubation, the medium was exchanged for the phenol red-free one and irradiated or kept in the dark. After irradiation, 2′,7′-dichlorofluorescein diacetate (DCF-DA, 10 μM) was added and kept in an incubator for 30 min. Then, the medium was carefully aspirated and fluorescence was measured. Excitation/emission wavelengths were 488/525 nm.

Uptake

HeLa cells were seeded in a 12-well plate in the full medium. The cells were treated with **2** the next day and incubated with the indicated concentrations and time. Then, the wells were washed with PBS, trypsinized, and analyzed by flow cytometry (BD FACSaria III). Excitation wavelength was 405 nm and emission wavelength was 655–685 nm.

Confocal microscopy

HeLa cells were seeded in a 96-well plate with a glass bottom (Cellvis) in the full medium. Cells were treated with **1** or **2** the next day and incubated for 24 h. An Andor xD spinning disc confocal microscope on an Olympus platform was used. The samples were activated by 405 nm laser light.

Radiotoxicity

Experiments were performed 24 h after seeding. The medium was exchanged for the phenol red-free full medium and **1** or **2** dissolved in water was added to a total concentration of 65 and 1300 μg mL^{-1}, respectively. After 24 h, the cells were irradiated using a X-RAD 225XL X-ray source (Precision X-RAY, Inc.) with an upper energy limit of 225 keV. Cell viability was measured by the resazurin assay (Sigma-Aldrich) after seeding at 10-times lower density and proliferation for 72 h. In control experiments, the cells were treated with water instead of **2**, otherwise the experimental conditions were the same.

Results and discussion

Synthesis and characterization

Precursor poly(HPMA-*co*-MA-β-Ala-DBCO) with 8 mol% of DBCO showed $M_w \approx 44\,000$ g mol^{-1}, narrow dispersity below 1.2, and a hydrodynamic size around 8 nm. Cluster/polymer conjugate **2** was prepared by a copper-free click reaction between the precursor's DBCO groups and the azido ligands of **1** as previously reported.[20] We used a large molar excess of **1** to promote the reaction of all DBCO reactive groups, ensuring the saturation of the polymer backbone with Mo_6 clusters and preventing crosslinking within the polymer. ICP-MS analysis of the samples revealed a molybdenum mass content of 10.7% which corresponds to a 35.1% mass content of **1** in conjugate **2**. Note that the use of precursors with higher DBCO contents (prepared up to 16 mol% of DBCO) led to conjugates with poor water solubility, evidently due to the increase of their hydrophobic character. Therefore, conjugate **2** only has the optimal composition for biological applications, *i.e.*, the highest content of Mo_6 cluster possible, while keeping good solubility.

Table 1 Mean sizes by number and zeta potentials of **1** and **2** for fresh and 8 day old PBS dispersions as obtained by dynamic light scattering

Sample	Age (days)	Mean size by number (nm)	ZP (mV)
1	0	22.7 ± 7.5	−17.7 ± 2.2
	8	n.a.	−15.3 ± 0.1
2	0	8.4 ± 1.9	−4.1 ± 1.0
	8	10.7 ± 2.3	−3.9 ± 1.4

The dispersions of **2** in PBS, a relevant medium in the context of biological applications, were measured by dynamic light scattering (Table 1 and Fig. S1, ESI†), revealing nanoparticles with a mean size by number of 8.4 ± 1.9 nm and a corresponding zeta potential of −4.1 ± 1.0 mV. For comparison, in PBS, **1** formed nanoaggregates with a mean size by number of 22.7 ± 7.5 nm and a zeta potential of −17.7 ± 2.2 mV. The dispersions of **2** in PBS displayed long-term colloidal stability, with a slight increase of the mean size by number to 10.7 ± 2.3 nm after 8 days and no change in the zeta potential. For comparison, 8 days old PBS dispersions of **1** could not be measured by DLS due to the formation of large aggregates, connected with hydrolysis of the cluster ligands.[21]

Photophysical properties

The photophysical properties of **1** and **2** were studied in PBS and are summarized in Table 2. Both samples displayed intensive red emission originating from the triplet states with maxima at 692 and 696 nm for **1** and **2**, respectively (Fig. 2). Interestingly, the phosphorescence quantum yield of **2** in argon-saturated PBS was 0.35 ± 0.02, substantially higher than that of **1**. This increase can be attributed to the extended

Table 2 Photophysical properties of **1** and **2** in PBS[a]

Sample	Age (days)	λ_L (nm)	ϕ_L	τ_L (μs)	τ_{air} (μs)
1	0	692	0.25 ± 0.02	105	6.0[b]
	8	703	0.08 ± 0.02	73[b]	5.0[b]
2	0	696	0.35 ± 0.02	140	16.1[b]
	8	697	0.33 ± 0.02	137	17.3[b]

[a] λ_L – emission maximum (λ_{exc} = 400 nm); τ_L and τ_{air} – amplitude average phosphorescence lifetimes in oxygen-free and air-saturated PBS, respectively (λ_{exc} = 405 nm, λ_{em} = 700 nm); and Φ_L – phosphorescence quantum yields in oxygen-free solutions (λ_{exc} = 320–400 nm, experimental error of Φ_L is ±0.01). [b] Biexponential decay curves.

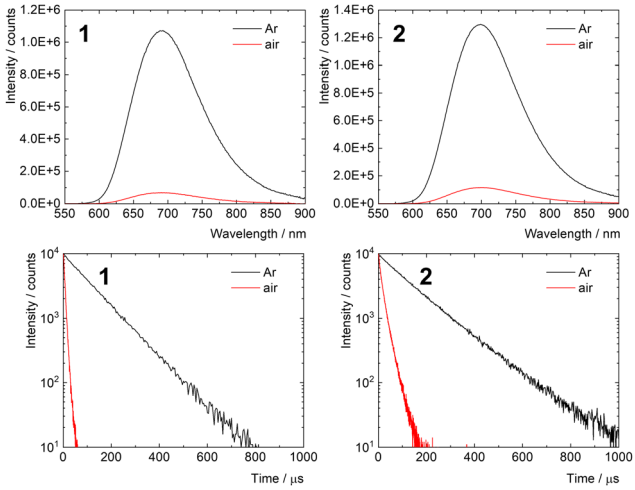

Fig. 2 Top: Phosphorescence emission spectra of **1** and **2**, excited at 400 nm. Bottom: Phosphorescence decay kinetics of **1** and **2** recorded at 700 nm, excited at 405 nm. Measurements were performed in argon- (black) and air- (red) saturated PBS.

shielding effect of the local environment within the conjugate, which reduces the vibrational quenching of the emissive triplet states in the presence of surrounding water molecules. Accordingly, the phosphorescence lifetime of **2** in argon-saturated PBS (140 μs) was also longer than that of **1** (105 μs). Strong decreases in the lifetimes of **1** and **2** were observed in air-saturated PBS (6.0 and 16.1 μs for **1** and **2**, respectively), when compared with those recorded in the absence of oxygen, indicating fast quenching of the corresponding triplet states by oxygen. This feature suggests the production of $O_2(^1\Delta_g)$, which was confirmed by measuring its NIR phosphorescence band centered around 1270 nm (Fig. S2, ESI†). The results demonstrate that the photosensitizing ability of **1** is preserved after conjugation with the polymer backbone. Even though the quantum yields of $O_2(^1\Delta_g)$ production in PBS were not quantified, the fraction of triplet states produced that are quenched in an air atmosphere P_T^{O2} ($P_T^{O2} = 1 - \tau_{air}/\tau_L$) was comparable for **1** (0.94) and **2** (0.86), suggesting similar $O_2(^1\Delta_g)$ production ability.

The stability of the photophysical properties was evaluated by comparing photophysical parameters of fresh and 8 day old PBS solutions. The experiments revealed a significant shift of the emission maximum and decrease of the phosphorescence quantum yield and lifetime for **1**, indicative of the hydrolytic process due to the limited coordination stability of **1** in aqueous media.[21] On the other hand, only minute changes within experimental error in these parameters were observed for **2**, highlighting the protective effect of the polymer backbone against hydrolysis of the cluster in a biological medium (Fig. S3, ESI†).

Cellular toxicity and phototoxicity

The biological activity of **1** and **2** was evaluated on human cervical carcinoma cells (HeLa cells). No dark toxicity was evidenced for **2** after 24 h of incubation in the medium containing 5% FBS (Table 3 and Fig. 3A) with concentrations

Table 3 IC_{50} obtained for **1** and **2** on HeLa cells, in the dark or after 460 nm irradiation[a]

Sample	IC_{50}(dark)[b] (μg mL^{-1}/μM)	IC_{50}(light)[b] (μg mL^{-1}/μM)
1 (5% FBS)	220/116	38/20
2 (5% FBS)	>1300/242	100/19
1 (no FBS)	9.3/5	1.2/0.63
2 (no FBS)	68/13	1.9/0.35

[a] After 24 h of incubation with 5% FBS or without FBS. [b] Concentration of Mo_6 cluster.

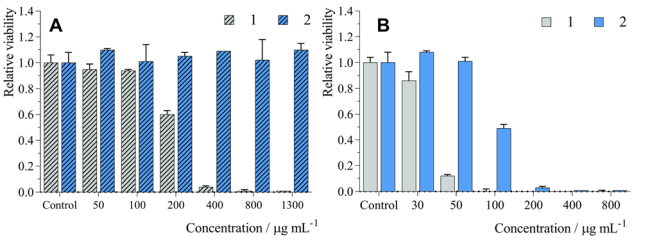

Fig. 3 Toxicity of **1** and **2** toward HeLa cells with the indicated concentrations in a full medium (5% FBS): (A) dark toxicity, 24 h incubation; (B) phototoxicity, 24 h incubation, and illuminated with 460 nm light (18 mW cm^{-2}, 15 min).

of up to 1300 μg mL^{-1} (*i.e.*, 242 μM in Mo_6 cluster), while **1** showed significant toxicity with an IC_{50} of 220 μg mL^{-1} (116 μM). Viability experiments were also performed in the absence of FBS during incubation with **1** or **2** in order to evaluate the effects of serum proteins on dark toxicity (Table 3 and Fig. S4, ESI†). After 24 h loading, we observed stronger dark toxicity with an IC_{50} of 9.3 μg mL^{-1} (5 μM) and 68 μg mL^{-1} (13 μM) for **1** and **2**, respectively. Probably, the difference between serum and serum-free media is due to the interaction of the conjugates with proteins such as albumin, which limit their cellular uptake.[22] Overall, conjugation of **1** with the polymer backbone led to a noticeably better therapeutic window, which is crucial for avoiding side-effects during RDT treatment that usually necessitates a high concentration of RSs.

In the case of phosphorescent Mo_6 clusters, phototoxicity is a pertinent preliminary indicator for evaluation of their potential as an RS.[12,16] Irradiation of HeLa cells incubated under the same conditions led to strong phototoxic effects with an IC_{50} of 38 μg mL^{-1} (20 μM) and 100 μg mL^{-1} (19 μM) for **1** and **2**, respectively (Table 3 and Fig. 3B). Similar to the dark toxicity, phototoxicity was greatly increased when incubation was performed in the absence of FBS, with IC_{50} of 1.2 μg mL^{-1} (0.63 μM) and 1.9 μg mL^{-1} (0.35 μM) for **1** and **2**, respectively (Table 3 and Fig. S4, ESI†), consistent with their better cellular uptake. Thus, conjugation of the Mo_6 cluster with the polymer led to the preservation of its phototoxicity, albeit lower than the phototoxicity of previously reported photosensitizing systems based on pure Mo_6 clusters. However, pure Mo_6 clusters have limited water solubility and, in some cases, limited stability in an aqueous environment, which can hamper their real therapeutic applications.[14,15]

Cell death and formation of ROS

The analysis of photoinduced cellular death pathways of **1** and **2** showed that HeLa cells undergo apoptosis, which is an advantageous process because it does not trigger inflammation like necrosis or necroptosis (Fig. 4A).[23]

ROS produced by a sensitizer cause oxidative damage to cells, which in turn brings cellular death. Since cancer cells upregulate their antioxidant and antiapoptotic systems when compared to healthy cells,[24] we investigated the formation of ROS by **1** and **2** in the cell culture using the DCF-DA assay. Irradiation of HeLa cells followed by the addition of DCF-DA led to a significant increase in detected ROS when compared to dark control experiments, in line with the dark/phototoxicity experiments (Fig. 4B and C).

Uptake and localization

For an effective RDT treatment, radiosensitizing nanosystems should enter targeted cells or interact with cell membranes, as the radial diffusion distance of the produced $O_2(^1\Delta_g)$ is approximately 150 nm from its point of production in aqueous media, which is enough to perturb cells.[25] The cellular uptake of **2** was investigated by flow cytometry in the 100–400 μg mL^{-1} concentration range where a linear time and dose-dependent uptake were observed (Fig. 5A, B and Fig. S5, ESI†). Interestingly, **2** was localized in the cell cytoplasm (Fig. 5C), similar to previously reported Mo_6@PLGA-PEG nanoparticles,[26] but also in the lysosomes as already reported for pure Mo_6 clusters (Fig. 5D).[14,27] Note that **1** exhibited similar cellular localization features (Fig. S6, ESI†), which substantiate the comparable photodynamic efficiency of **1** and **2**.

Radiotoxicity

The presence of RSs can enhance the radiosensitivity of tumor cells, thus increasing the efficacy of radiotherapy. Apart from the radiolysis of water, which is a primary absorber of X-ray radiation, the radiation effects can be enhanced in the presence of heavy elements as high *Z*-atoms have considerably higher photoelectric cross sections than soft tissues. Thus, radiosensitization is based on the ionizing effects of photoelectrons, Compton electrons, Auger electrons, and fluorescence photons on their immediate environment (water, oxygen, biomolecules, or RS materials), which directly damage biomolecules or indirectly destroy biomolecules by generated free radicals, mostly by ROS. ROS induce chemical reactions with biomolecules, such as oxidation of bases, crosslinking of biomolecules, peroxidation of fatty acids, or disbalancing the cell redox system, which could result in cell death.

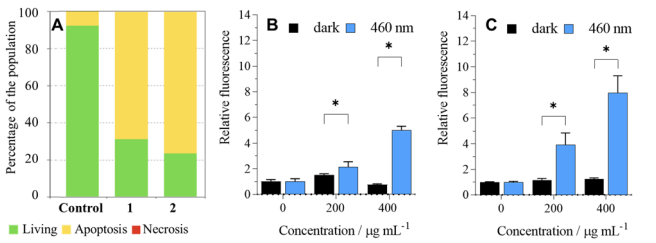

Fig. 4 (A) Apoptotic, necrotic, and living HeLa cell populations after incubation with **1** or **2** at a concentration of 200 μg mL^{-1}, for 24 h in the dark and then irradiation by 460 nm light. (B) Formation of ROS in HeLa cells using the indicated concentration of **1** after PDT treatment, 10 μM DCF-DA. (C) Formation of ROS in HeLa cells using the indicated concentration of **2** after PDT treatment, 10 μM DCF-DA; * represents statistically significant differences according to the Students's *t*-test ($p < 0.05$).

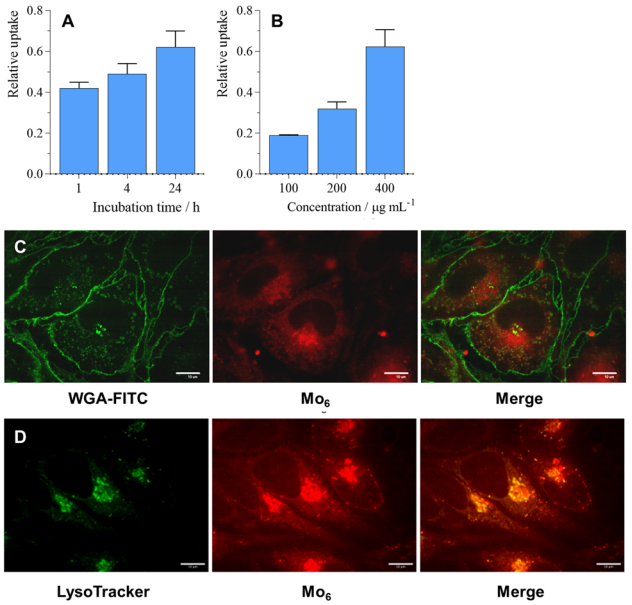

Fig. 5 Uptake of **2** in HeLa cells: (A) 400 μg mL^{-1}, incubation times up to 24 h; (B) various concentrations of **2**, 24 h incubation. The results were normalized to the highest response; (C) cellular colocalization of **2** in HeLa cells obtained by confocal laser scanning microscopy (WGA-FITC, green: cell membrane; Mo_6, red: cluster; and merge: cell membrane and cluster together); (D) cellular colocalization of **2** in HeLa cells obtained by confocal laser scanning microscopy (LysoTracker, green: lysosomes; Mo_6, red: cluster; and merge: lysosomes and cluster together). White bars represent 10 μm.

Our previous studies have demonstrated the potential of Mo_6 clusters for RDT. Therefore, the presented nanosystem was evaluated as an RS by performing an experiment on HeLa cells, where cells were incubated with **2** at a non-toxic concentration of 1300 μg mL^{-1} for 24 h. Cell proliferation was monitored after their irradiation with X-ray doses of 8 and 10 Gy (Fig. 6). Under these conditions, a significant suppression of the cell growth was observed compared to the irradiated control in the absence of **2**. For comparison, no detectable radiotoxic effect was evidenced for **1** at its maximum non-toxic concentration of 65 μg mL^{-1} (Fig. S7, ESI†). Thus, the wider therapeutic window of the conjugated cluster allows for the use of a higher incubation concentration necessary to trigger a significant radiosensitizing effect. The dose enhancement factor of **2** was approximately 1.4, comparable to that of gold nanoparticles,[28,29] albeit lower than that of pure Mo_6 clusters, which usually exhibit remarkable cellular uptake properties, but have delivery limitations for therapeutic applications.[12,16]

Conclusions

This article presents the design of functional Mo_6 cluster/*N*-(2-hydroxypropyl)methacrylamide copolymer click-conjugates for

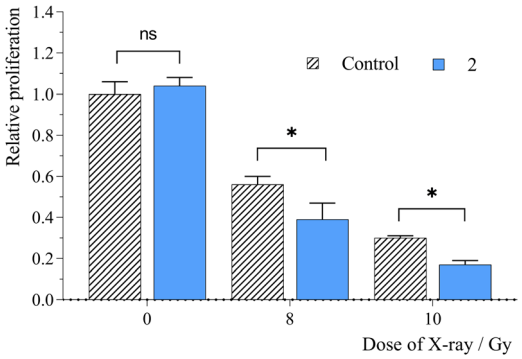

Fig. 6 Radiotoxicity of **2** towards HeLa cells using an incubation concentration of 1300 μg mL^{-1}, 24 h incubation in the full medium (5% FBS), and irradiated with an X-RAD 225XL X-ray source (upper energy limit is 225 keV); * represents statistically significant differences according to the Students's *t*-test ($p < 0.05$); ns stands for non significant differences.

radiodynamic applications. The conjugate formed nanoparticles of suitable sizes and zeta potentials for biological applications, and demonstrated long-term colloidal stability in PBS and enhanced stability of the photophysical properties. Importantly, while bare cluster **1** exhibited significant toxicity, conjugate **2** showed no cellular toxicity towards HeLa cells after 24 h of incubation, leading to a wider therapeutic window. This feature is crucial for radiodynamic applications where the dose of radiosensitizer delivered to tumour cells should be high and non-toxic. The conjugate was tested as an RS in RDT, showing a significant suppression of cell growth upon X-ray irradiation comparable to that of gold nanoparticles. Overall, the study highlights the therapeutic potential of Mo_6 clusters for photo/radiodynamic applications. Further studies are planned to reach specific cancer cells targeting by exploiting the remaining unreacted azido groups of the clusters for click addition of targeting moieties such as antibodies or aptamers.

Author contributions

Conceptualization (R. P., K. K., M. R. T., and K. L.), supervision (T. E, K. L, and T. R.), investigation (R. P, K. K, M. R. T., M. P., T. P., and I. K.), writing – original draft (R. P., K. K., and T. P.), writing – review and editing (T. E., J. Z., and K. L.), project administration (T. E., T. R., and K. L.), and funding acquisition (T. E., T. R., and K. L.).

Conflicts of interest

There are no conflicts to declare.

Acknowledgements

The authors are grateful to the Czech Science Foundation (No. 21-11688S). This work was supported by the National Institute for Cancer Research (Program EXCELES, ID Project No. LX22NPO5102) funded by the European Union – Next Generation EU.

Notes and references

1 W. Chen and J. Zhang, *J. Nanosci. Nanotechnol.*, 2006, **6**, 1159–1166.
2 L. Larue, A. Ben Mihoub, Z. Youssef, L. Colombeau, S. Acherar, J. C. André, P. Arnoux, F. Baros, M. Vermandel and C. Frochot, *Photochem. Photobiol. Sci.*, 2018, **17**, 1612–1650.
3 W. Sun, Z. Zhou, G. Pratx, X. Chen and H. Chen, *Theranostics*, 2020, **10**, 1296–1318.
4 A. Bulin, M. Broekgaarden, F. Chaput, V. Baisamy, J. Garrevoet, B. Busser, D. Brueckner, A. Youssef, J. Ravanat, C. Dujardin, V. Motto-Ros, F. Lerouge, S. Bohic, L. Sancey and H. Elleaume, *Adv. Sci.*, 2020, **7**, 2001675.
5 G. Zhang, M. Guo, H. Ma, J. Wang and X.-D. Zhang, *Biomater. Sci.*, 2023, **11**, 1153–1181.
6 K. Kirakci, M. A. Shestopalov and K. Lang, *Coord. Chem. Rev.*, 2023, **481**, 215048.
7 C.-C. Yang, Y.-J. Sun, P.-H. Chung, W.-Y. Chen, W. Swieszkowski, W. Tian and F.-H. Lin, *Ceram. Int.*, 2017, **43**, 12675–12683.
8 Y. Chen, J. Yang, S. Fu and J. Wu, *Int. J. Nanomed.*, 2020, **15**, 9407–9430.
9 K. Kirakci, P. Kubát, K. Fejfarová, J. Martinčík, M. Nikl and K. Lang, *Inorg. Chem.*, 2016, **55**, 803–809.
10 K. Kirakci, P. Kubát, J. Langmaier, T. Polívka, M. Fuciman, K. Fejfarová and K. Lang, *Dalton Trans.*, 2013, **42**, 7224.
11 K. Kirakci, T. N. Pozmogova, A. Y. Protasevich, G. D. Vavilov, D. V. Stass, M. A. Shestopalov and K. Lang, *Biomater. Sci.*, 2021, **9**, 2893–2902.
12 M. Koncošová, M. Rumlová, R. Mikyšková, M. Reiniš, J. Zelenka, T. Ruml, K. Kirakci and K. Lang, *J. Mater. Chem. B*, 2022, **10**, 3303–3310.
13 K. Kirakci, J. Zelenka, M. Rumlová, J. Cvačka, T. Ruml and K. Lang, *Biomater. Sci.*, 2019, **7**, 1386–1392.
14 K. Kirakci, J. Demel, J. Hynek, J. Zelenka, M. Rumlová, T. Ruml and K. Lang, *Inorg. Chem.*, 2019, **58**, 16546–16552.
15 K. Kirakci, M. Kubáňová, T. Přibyl, M. Rumlová, J. Zelenka, T. Ruml and K. Lang, *Inorg. Chem.*, 2022, **61**, 5076–5083.
16 K. Kirakci, J. Zelenka, M. Rumlová, J. Martinčík, M. Nikl, T. Ruml and K. Lang, *J. Mater. Chem. B*, 2018, **6**, 4301–4307.
17 X. Xiao, F. Teng, C. Shi, J. Chen, S. Wu, B. Wang, X. Meng, A. Essiet Imeh and W. Li, *Front. Bioeng. Biotechnol.*, 2022, **10**, DOI: 10.3389/fbioe.2022.1024143.
18 S. Kotta, H. M. Aldawsari, S. M. Badr-Eldin, A. B. Nair and K. Yt, *Pharmaceutics*, 2022, **14**, 1636.
19 Y. Shi, R. van der Meel, X. Chen and T. Lammers, *Theranostics*, 2020, **10**, 7921–7924.
20 M. R. Tavares, K. Kirakci, N. Kotov, M. Pechar, K. Lang, R. Pola and T. Etrych, *Nanomaterials*, 2022, **12**, 3350.
21 K. Kirakci, P. Kubát, M. Kučeráková, V. Šícha, H. Gbelcová, P. Lovecká, P. Grznárová, T. Ruml and K. Lang, *Inorg. Chim. Acta*, 2016, **441**, 42–49.
22 K. Yamasaki, V. T. G. Chuang, T. Maruyama and M. Otagiri, *Biochim. Biophys. Acta, Gen. Subj.*, 2013, **1830**, 5435–5443.
23 Z. Liu and D. Jiao, *Cell Stress*, 2020, **4**, 1–8.
24 J. Zelenka, M. Koncošová and T. Ruml, *Biotechnol. Adv.*, 2018, **36**, 583–602.
25 P. R. Ogilby, *Chem. Soc. Rev.*, 2010, **39**, 3181–3209.

26 A. Verger, G. Dollo, N. Brandhonneur, S. Martinais, S. Cordier, K. Lang, M. Amela-Cortes and K. Kirakci, *Mater. Adv.*, 2023, **4**, 3207–3214.
27 K. Kirakci, J. Zelenka, I. Křížová, T. Ruml and K. Lang, *Inorg. Chem.*, 2020, **59**, 9287–9293.
28 X.-D. Zhang, D. Wu, X. Shen, J. Chen, Y.-M. Sun, P.-X. Liu and X.-J. Liang, *Biomaterials*, 2012, **33**, 6408–6419.
29 D. B. Chithrani, S. Jelveh, F. Jalali, M. van Prooijen, C. Allen, R. G. Bristow, R. P. Hill and D. A. Jaffray, *Radiat. Res.*, 2010, **173**, 719.